Cell-alignment patterns in the collective migration of cells with polarized adhesion

Katsuyoshi Matsushita
Department of Biological Sciences, Osaka University, Toyonaka, Osaka, Japan
(Received 7 March 2016; revised manuscript received 1 March 2017; published 24 March 2017)

Dictyostelium discoideum (Dd) utilizes inhomogeneities in the distribution of cell-cell adhesion molecules on cell membranes for collective cell migration. A simple example of an inhomogeneity is a front-side (leading-edge) polarization in the distribution at the early streaming stage. Experiments have shown that the polarized cell-cell adhesion induces side-by-side contact between cells [Beug *et al.*, Nature (London) **274**, 445 (1978)]. This result is counterintuitive, as one would expect cells to align front to front in contact with each other on the basis of front-side polarization. In this work, we theoretically examine whether front-side polarization induces side-by-side contact in collective cell migration. We construct a model for expressing cells with this polarization based on the two-dimensional cellular Potts model. By a numerical simulation with this model, we find cell-cell alignment wherein cells form lateral arrays with side-by-side contacts as observed in the experiments.

DOI: 10.1103/PhysRevE.95.032415

I. INTRODUCTION

Collective cell migration is widely observed in the development of organisms and is indispensable for the morphogenesis therein [1–3]. In this decade, collective cell migration has been intensively investigated in the fields of applied mathematics and theoretical physics [4–10]. These investigations contribute to the description of various collective cell migrations. However, an understanding of the fundamental mechanisms guiding cells in such migrations has not been sufficiently achieved to date because of the complexity and diversity of biological systems. In fact, this complexity and diversity have resulted in many hypotheses on the guidance mechanism for collective cell migration [11]. Most of the deeper theoretical examinations necessary to support physical aspects of these hypotheses have yet to be undertaken.

Cell-alignment patterns in collective cell migrations reflect their guidance mechanism. A theoretical explanation of such patterns would provide an effective means of supporting a hypothesis for the guidance mechanism. The patterns originate from various features of cells, including chemotaxis [12], cell-level motility [13], cell-cell adhesion [14], and cell-extracellular matrix interaction [15]. In any theoretical explanation, an important issue will be the clarification of the relationship between these features and the relevant patterns.

In clarifying this relationship, theoretical modeling that ideally focuses on a particular cell feature is useful for avoiding the complexity of biological systems. In the present work, we focus on the feature of cell-cell adhesion, motivated by the fact that cell-cell adhesion is a steering factor in cell coordination and hence significantly affects the patterns formed [16–18]. Cell-cell adhesion in collective cell migration has been well investigated for *Dictyostelium discoideum* (Dd) [19] and has been reported to promote cell-alignment pattern formation [20,21]. We further narrow our focus to the cell-cell adhesion of Dd. This narrowing allows us to avoid complicating our discussion with matters that are due to the diversity of biological systems. Using the rich insights into Dd, we discuss the relationship between cell-alignment patterns and cell-cell adhesion.

Investigations to date have identified three molecules in cell-cell adhesion [22]. These molecules control the fruiting body formation of starved Dd [23]. Their expression changes with the progress of the fruiting body formation. First, the expression of gp24/DdCAD-1 [24,25] is observed with the streaming formation of Dd in a very early stage. Then, as the streaming formation proceeds, the expression of another molecule, gp80/csA [26,27], becomes prominent. Lastly, the heterophilic molecule pair TgrB1-LagC/gp150/TgrC1 is expressed with the formation of cell aggregation [28,29]. These molecules are distributed on the cell membrane and stabilize cell-cell contact in various ways [26,30]. The variety in the styles of cell-cell contact results from the notable fact that the concentration of cell-cell adhesion molecules exhibits various spatial inhomogeneities.

We focus on gp24/DdCAD-1 as an example of these inhomogeneities. Experiments on Dd have found that the localization of this molecule is strongly polarized at the front side (leading edge) of the cell as shown in Fig. 1(a) [19,31]. The molecule induces side-by-side contact of cells in streaming motions as shown in Fig. 1(b) and promotes their alignments [26,30]. These results seem counterintuitive, as one would expect cells to align front to front as shown in Fig. 1(c) owing to the localization of the adhesion protein. In the present work, we investigate whether cell motility along with this polarized cell-cell adhesion can explain the alignment of nearby cells.

The present work is intended to shed light on the mechanism of side-by-side contact. In this work, we propose the hypothesis that the contact is an emergent effect of the synergy between polarized cell-cell adhesion and cell motility. This hypothesis offers a different point of view, namely, that of the synergy between cell-cell adhesion and cell motility, and may thereby provide a deeper understanding of the guidance mechanism for collective cell migration.

To this end, we develop a model based on the two-dimensional (2D) cellular Potts model [32,33]. The model is extended to express this polarized cell-cell adhesion on the basis of the inhomogeneous concentration of adhesion molecules. Through a numerical simulation using this model, we demonstrate that cells form lateral arrays through side-by-side contact in their collective migration. This result supports our hypothesis for side-by-side contact and explains the cell-alignment pattern observed in experiments [26,30].

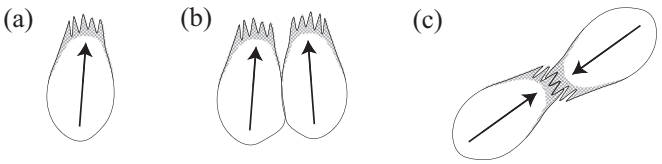

FIG. 1. (a) Schematic image of a *Dictyostelium discoideum* cell in the early streaming stage. Darkened areas indicate regions where the concentration of the adhesion molecule gp24/DdCAD-1, $\rho(\boldsymbol{r})$, is high. Arrows represent the direction of cell polarity leading its motion $\boldsymbol{\mu}$ and the sawtooth shape at the front of the cell represents pseudopods. (b) Side-by-side contact between two cells. (c) Front-to-front contact between two cells.

In addition to the cellular Potts model, many theoretical models have been used to express collective cell migration. We briefly review these models in order to clarify the appropriateness of our choice of model. Since the Keller-Segel model was developed to explain Dd aggregation about half a century ago [33–36], various continuum theoretical models have been applied to collective cell migration including those of wound healing [5,6,37] and epithelial spreading [38,39]. In recent years, sophisticated continuum models including phase field models opened a different approach for expressing details of cell features. Such a model provided a detailed reproduction of the migration of fish keratocytes [40,41] and has been further applied to collective cell migration [42–45]. Models of another type, discrete particle models, have also been frequently used for expressing collective cell migration including swarming of keratocytes [4] and wound healing [46]. These models provide a possible tool for analyzing the collective behavior of many-cell systems [47,48]. Furthermore, reflecting the diversity of biological systems, hybrid variants of these models [49,50] and many other types of models [51–55] have been developed to express the specificity of biological systems.

In the present work, from these models, we adopt the cellular Potts model. The cellular Potts model has been conventionally used for the reproduction of cell-alignment patterns in Dd due to cell-cell adhesion [20]. This use is due to the following advantage: in comparison with other models, the model is relatively simple to use to express cell-cell adhesion-inducing phenomena such as cell sorting [32]. This advantage has enabled this model to be widely applied to more complex systems including the final stage of fruiting body formation [56], root growth [57], T-cell migration in lymph nodes [58], vasculogenesis [59], and tumor growth [60]. Furthermore, this model has the flexibility to express polarization in cell-cell adhesion [61,62] and is therefore appropriate for our purpose.

Here, we briefly summarize the organization of this paper. Section II is devoted to an explanation of our model, with three subsections: Sec. II A provides a basic description of the cellular Potts model; Sec. II B explains the key of our model, the formulation of polarized cell-cell adhesion, which is based on the inhomogeneity of the concentration of adhesion molecules; and Sec. II C explains the dynamics of the cell polarity that controls cell motility. Next, in Sec. III, our simulation results are described in four subsections as follows: Sec. III A briefly revisits investigations of the case without polarized cell-cell adhesion to determine the parameters of our simulation; for the case with polarized cell-cell adhesion, Secs. III B and III C examine the criteria for collective cell migration (mechanical cell-cell contacts and supracellular polarity, respectively); and Sec. III D demonstrates side-by-side contact via this model and therewith evaluates our hypothesis. Finally, Sec. IV explains the mechanism of side-by-side contact formation and gives related remarks.

II. MODEL

In this section, we explain our model. This model is constructed on the basis of the 2D cellular Potts model.

A. Cellular Potts model

This subsection describes the 2D cellular Potts model. The two-dimensionality of this model corresponds to a scenario in which the cells are cultured cells on a 2D medium and do not form 3D structures; this is the case in a typical experimental setting for Dd in the early stages of fruiting body formation.

The cellular Potts model simulates probable cell configurations. First, we explain how to express cell configurations in this model. For this explanation, let us consider the cell configuration shown in the left panel of Fig. 2(a). In this model, this configuration is represented by a state of the 2D Potts model [63] on a square lattice as shown in the right panel of Fig. 2(a). A state is denoted by $\{m(\boldsymbol{r})\}$. The brackets $\{\dots\}$ denote a set of numbers defined at all the sites $\boldsymbol{r}$ in the square lattice. $m(\boldsymbol{r})$ denotes the Potts state at the site $\boldsymbol{r}$. $m(\boldsymbol{r})$ takes a number in $\{0,1,2,\dots,N_{\mathrm{Cell}}\}$, where N_{Cell} is the number of cells, and represents the index of the cell that occupies $\boldsymbol{r}$. Hence, for a given $\{m(\boldsymbol{r})\}$, the domain of $m(\boldsymbol{r})=m$ represents the shape of the mth cell. $m(\boldsymbol{r})=0$ represents the special case that the site $\boldsymbol{r}$ is empty. In the present simulation, N_{Cell} is assumed to be constant for simplicity. This assumption is made for representing the early stage of the streaming of Dd, where cells rarely proliferate and also rarely die during experiments.

Next, we go on to a description of the probability of realization for $\{m(\boldsymbol{r})\}$, denoted as $P(\{m(\boldsymbol{r})\})$. With this probability, one can sample for a probable cell configuration by using Monte Carlo simulation and thereby simulate cell configurations. $P(\{m(\boldsymbol{r})\})$ is represented by the Boltzmann weight $P(\{m(\boldsymbol{r})\}) \propto \exp[-\beta\mathcal{H}(\{m(\boldsymbol{r})\})]$. β is an inverse temperature, which characterizes cell motility [64]. $\mathcal{H}$ is energy consisting of three terms as follows:

$$\mathcal{H}(\{m(\boldsymbol{r})\})=\mathcal{H}_{\mathrm{a}}(\{m(\boldsymbol{r})\})+\mathcal{H}_{\mathrm{v}}(\{m(\boldsymbol{r})\})+\mathcal{H}_{\mathrm{m}}(\{m(\boldsymbol{r})\}). \quad (1)$$

The first term on the right side of Eq. (1) represents both the tension of the cell periphery and the cell-cell adhesion [64,65]. The concrete expression is given by

$$\mathcal{H}_{\mathrm{a}}(\{m(\boldsymbol{r})\}) = \sum_{\langle \boldsymbol{r},\boldsymbol{r}'\rangle} J_{m(\boldsymbol{r})m(\boldsymbol{r}')}[1-\delta_{m(\boldsymbol{r})m(\boldsymbol{r}')}]. \quad (2)$$

$\langle \boldsymbol{r},\boldsymbol{r}'\rangle$ in the summation indicates that the summation is taken over all adjacent site pairs. The set of adjacent sites consists of all the nearest neighbor sites and the second-nearest neighbor sites; this choice for adjacent sites reduces the artificial effects of discreteness in the lattice [32].

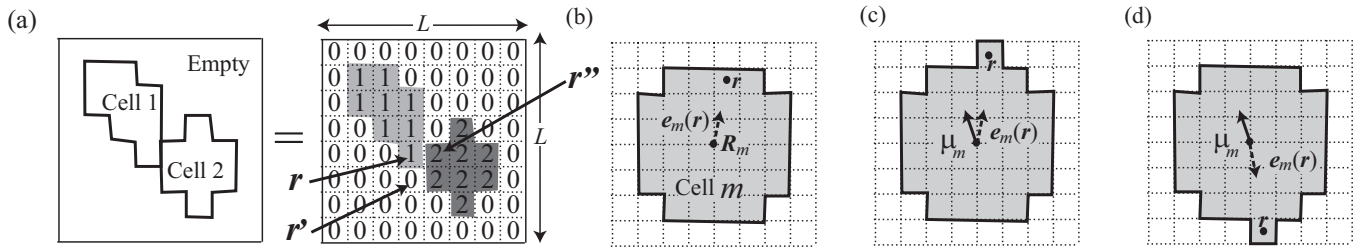

FIG. 2. (a) Schematic image of the correspondence between the configuration of cells and a Potts state. The left panel represents the configuration of two cells ($N_{\rm Cell} = 2$) in an empty space. The right panel shows the corresponding Potts state. L is the linear size of the system, and $\boldsymbol{r}$, $\boldsymbol{r}'$, and $\boldsymbol{r}''$ are neighboring sites occupied by cell 1, the empty space, and cell 2, respectively. (b) $\boldsymbol{e}_m(\boldsymbol{r})$, representing the unit vector from the central position $\boldsymbol{R}_m$ of cell m to a peripheral site $\boldsymbol{r}$. The dashed arrow represents the direction of $\boldsymbol{e}_m(\boldsymbol{r})$. (c) A favorable pseudopod formation at $\boldsymbol{r}$ given the configuration in (b) and the propulsion direction of cell m, indicated by the unit vector $\boldsymbol{\mu}_m$ (solid arrow). (d) An unfavorable pseudopod formation at $\boldsymbol{r}$ given the configuration in (b) and the propulsion direction of cell m, indicated by the unit vector $\boldsymbol{\mu}_m$ (solid arrow).

$\delta_{mm'}$ in (2) and hereinafter is the Kronecker δ,

$$\delta_{mm'} = \begin{cases} 1 & m = m' \\ 0 & m \neq m' \end{cases}. \tag{3}$$

Hence, for each adjacent site pair $\boldsymbol{r}$ and $\boldsymbol{r}'$, Eq. (2) gives a positive value only at the domain boundary, $m(\boldsymbol{r}) \neq m(\boldsymbol{r}')$. Equation (2) gives no effect when $m(\boldsymbol{r}) = m(\boldsymbol{r}')$.

The surface energy, $J_{mm'}$ in Eq. (2), depends on m and m' as follows:

$$J_{mm'} = \begin{cases} J_{\rm CE} & m = 0 \text{ or } m' = 0 \\ J(\rho_m(\boldsymbol{r}), \rho_{m'}(\boldsymbol{r}')) & m \neq 0 \text{ and } m' \neq 0 \end{cases}, \tag{4}$$

where $J_{\rm CE}$ represents the tension of the cell periphery in the empty space, and $J(\rho_m(\boldsymbol{r}), \rho_{m'}(\boldsymbol{r}'))$ is the adhesion energy, in which $\rho_m(\boldsymbol{r})$ represents the concentration of adhesion molecules on the periphery site $\boldsymbol{r}$ of the mth cell.

To demonstrate how this dependence represents both the tension of the cell periphery and the cell-cell adhesion, we consider a site $\boldsymbol{r}$ occupied by cell 1 as shown in Fig. 2(a). In this case, $m(\boldsymbol{r}) = 1$. The site lies next to adjacent $\boldsymbol{r}'$, which is an empty space represented by $m(\boldsymbol{r}') = 0$. In this case, $J_{m(\boldsymbol{r})m(\boldsymbol{r}')}$ is a constant, $J_{\rm CE}$, defined as the tension of the cell periphery in the empty space. As shown in Fig. 2(a), the site $\boldsymbol{r}$ also lies next to adjacent site $\boldsymbol{r}''$, which is occupied by cell 2, represented by $m(\boldsymbol{r}'') = 2$. In this case, $J_{m(\boldsymbol{r})m(\boldsymbol{r}'')} = J(\rho_1(\boldsymbol{r}), \rho_2(\boldsymbol{r}''))$, which defines the adhesion energy representing the adhesion between cells 1 and 2. Through this dependence, Eq. (2) represents both the tension of the cell periphery and the cell-cell adhesion.

$\rho_m(\boldsymbol{r})$ in Eq. (4) represents the concentration of adhesion molecules at the periphery site $\boldsymbol{r}$ of the mth cell. Hence, the expression for the adhesion energy, $J(\rho_m(\boldsymbol{r}), \rho_{m'}(\boldsymbol{r}'))$, means that it is a function of the concentration of adhesion molecules. This function form for $J(\rho_m(\boldsymbol{r}), \rho_{m'}(\boldsymbol{r}'))$ is not the conventional representation for polarization in cell-cell adhesion. We discuss the concrete function form separately in the next subsection in order to avoid redundancy in this explanation of $P(\{m(\boldsymbol{r})\})$.

The second term on the right side of Eq. (1) is introduced to represent the empirical fact that the cell volume is almost constant. The expression is

$$\mathcal{H}_{\rm v}(\{m(\boldsymbol{r})\}) = \kappa \sum_{m=1}^{N_{\rm Cell}} (V_m - V)^2, \tag{5}$$

where κ is the cell volume stiffness [32], V_m represents the volume of the mth cell, namely, $V_m = \sum_{\boldsymbol{r}} \delta_{mm(\boldsymbol{r})}$, and V denotes the maintenance target value for the volume.

The last term on the right side of Eq. (1) represents the self-propulsion of the cell. This term is expressed as

$$\mathcal{H}_{\rm m}(\{m(\boldsymbol{r})\}) = -E \sum_{m=1}^{N_{\rm Cell}} \sum_{\boldsymbol{r} \in \Omega_m} \boldsymbol{\mu}_m \cdot \boldsymbol{e}_m(\boldsymbol{r}); \tag{6}$$

E is the magnitude of the self-propulsion. Ω_m is the set of all sites occupied by the mth cell. $\boldsymbol{\mu}_m$ is a unit vector indicating the propulsion direction of the mth cell [39]. For simplicity, we call this direction "cell polarity", following conventional terminology [66]. In this model, $\boldsymbol{\mu}_m$ is one of the degrees of freedom. We postpone the explanation of the dynamics of $\boldsymbol{\mu}_m$ to Sec. II C in order to avoid redundancy in this explanation of $P(\{m(\boldsymbol{r})\})$. As shown in Fig. 2(b), $\boldsymbol{e}_m(\boldsymbol{r})$ is a unit vector from $\boldsymbol{R}_m$ to $\boldsymbol{r}$, where $\boldsymbol{R}_m$ is the central position of the mth cell and is defined as

$$\boldsymbol{R}_m = \frac{1}{V_m} \sum_{\boldsymbol{r} \in \Omega_m} \boldsymbol{r}. \tag{7}$$

More concretely,

$$\boldsymbol{e}_m(\boldsymbol{r}) = \frac{\boldsymbol{r} - \boldsymbol{R}_m}{|\boldsymbol{r} - \boldsymbol{R}_m|}. \tag{8}$$

The intuitive interpretation of Eq. (6) is as follows: $\boldsymbol{\mu}_m$ represents the direction of the movement of the cell. Since Dd moves by forming pseudopods [23], $\boldsymbol{\mu}_m$ represents the direction in which the pseudopods tend to form. To represent this situation in $\mathcal{H}_{\rm m}(\{m(\boldsymbol{r})\})$, we use the energy proportional to the inner product of $\boldsymbol{\mu}_m$ by the vector $\boldsymbol{e}_m(\boldsymbol{r})$ as shown in Eq. (6). This represents the fact that the direction of pseudopod formation indicated by $\boldsymbol{e}_m(\boldsymbol{r})$ is favorably selected as it closely aligns with $\boldsymbol{\mu}_m$. For example, the pseudopod formation in Fig. 2(c) from the state shown in Fig. 2(b) is favorable because this formation reduces the energy. In contrast, pseudopod formation in the opposite direction as shown in Fig. 2(d) from the state shown in Fig. 2(b) is suppressed. Furthermore,

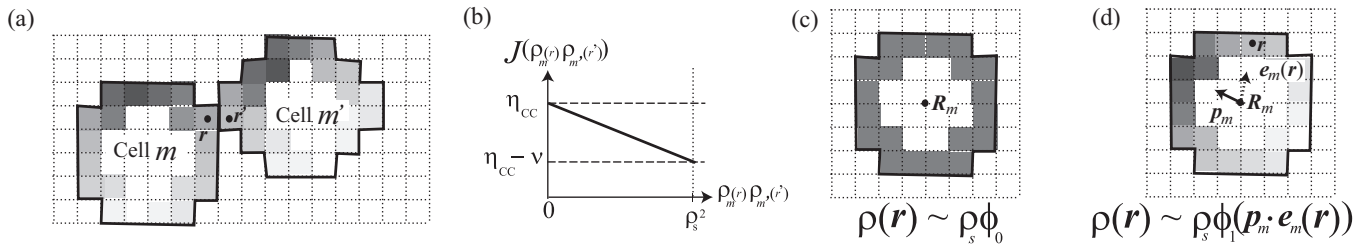

FIG. 3. Schematic images of adhesion molecule concentration $\rho(\boldsymbol{r})$ at cell periphery. Gray shades represent the adhesion molecule concentrations on the membrane: black indicates a high concentration, and white indicates a low concentration. (a) Adhesion contacts between the mth cell and the m'th cell. $\boldsymbol{r}$ represents a contacting site for the mth cell, and $\boldsymbol{r}'$ represents a contacting site for the m'th cell. (b) Excess energy of cell-cell adhesion, $J(\rho_m(\boldsymbol{r}),\rho_{m'}(\boldsymbol{r}'))$, as a function of the product of adhesion molecule concentrations, $\rho_m(\boldsymbol{r})\rho_{m'}(\boldsymbol{r})$. (c) Unpolarized component of adhesion molecule concentration. (d) Polarized component of adhesion molecule concentration. Vector $\boldsymbol{p}_m$ represents the polarization direction of the adhesion molecule concentration. Vector $\boldsymbol{e}_m(\boldsymbol{r})$ is a unit vector indicating a position $\boldsymbol{r}$ on the periphery of the mth cell. $\boldsymbol{R}_m$ and $\boldsymbol{r}$ represent the center position of the mth cell and a position on the cell periphery, respectively.

after $\boldsymbol{R}_m$ moves in the direction of $\boldsymbol{\mu}_m$ by the pseudopod formation, the domain of the mth cell is contracted in the direction opposite from $\boldsymbol{\mu}_m$ because the contraction reduces the energy. As a result, this term induces the self-propulsion of the cell in the direction of $\boldsymbol{\mu}_m$.

Up to this point, we have defined the probability of realization $P(\{m(\boldsymbol{r})\})$ for $\{m(\boldsymbol{r})\}$. Here, we move on to an explanation of the simulation method for sampling cell configurations by following $P(\{m(\boldsymbol{r})\})$. In this simulation, the following conventional Monte Carlo sampling process is employed. During this sampling process, a Monte Carlo step is iterated. In this Monte Carlo step, $16\times L^2$ copy trials of $m(\boldsymbol{r})$ are sequentially generated, where L represents the linear size of the system as shown in Fig. 2(a). For each copy trial, first the trial site $\boldsymbol{r}$ is randomly chosen. Then, the state $m_{\rm trial}(\boldsymbol{r}')$ of an adjacent site $\boldsymbol{r}'$ is selected randomly as the copy trial state, as in the voter model [67]. The copy of the trial state to the site $\boldsymbol{r}$ is accepted with a certain acceptance probability, given by the Metropolis transition probability,

$$P(\{m_{\rm trial}(\boldsymbol{r})\}|\{m(\boldsymbol{r})\})=\min\left[1,\frac{P(\{m_{\rm trial}(\boldsymbol{r})\})}{P(\{m(\boldsymbol{r})\})}\right], \tag{9}$$

where $\{m_{\rm trial}(\boldsymbol{r})\}$ is the configuration in which $m(\boldsymbol{r})$ in $\{m(\boldsymbol{r})\}$ is replaced with $m_{\rm trial}(\boldsymbol{r}')$. Finally, if the copy is accepted, $m(\boldsymbol{r})$ is replaced with $m_{\rm trial}(\boldsymbol{r}')$; otherwise, $m(\boldsymbol{r})$ remains.

This Monte Carlo step is iterated to produce a series of configurations $\{m(\boldsymbol{r})\}$, which can be sampled to obtain a probable cell configuration. Note that the series of sampled configurations is recognized as a time series of cell configurations; therefore, the simulation also accomplishes sampling for cell dynamics.

B. Polarized adhesion

The model in the previous subsection contains the surface energy, expressing the cell-cell adhesion $J(\rho_m(\boldsymbol{r}),\rho_{m'}(\boldsymbol{r}'))$, in Eq. (4). Since for our purpose $J(\rho_m(\boldsymbol{r}),\rho_{m'}(\boldsymbol{r}'))$ should express the polarized cell-cell adhesion of Dd, $J(\rho_m(\boldsymbol{r}),\rho_{m'}(\boldsymbol{r}'))$ should be appropriately formulated to reflect the inhomogeneity in the adhesion molecule concentrations $\rho_m(\boldsymbol{r})$ and $\rho_{m'}(\boldsymbol{r}')$. Here, as defined in the previous subsection, $\rho_m(\boldsymbol{r})$ is the concentration of adhesion molecules at site $\boldsymbol{r}$ on the periphery of the mth cell. In this subsection, we develop the appropriate formulation for $J(\rho_m(\boldsymbol{r}),\rho_{m'}(\boldsymbol{r}'))$.

To this end, we consider an adhesive contact between two cells. We assume that the contact is formed between the mth and m'th cells shown in Fig. 3(a). We concentrate on the contact localized at the interface between sites $\boldsymbol{r}$ and $\boldsymbol{r}'$. As mentioned above, $J(\rho_m(\boldsymbol{r}),\rho_{m'}(\boldsymbol{r}'))$ is supposed to depend on both $\rho_m(\boldsymbol{r})$ and $\rho_{m'}(\boldsymbol{r}')$. Since the adhesion molecules are necessary for both cells to form adhesive contact, we can expect that the strength of the adhesion depends on the product $\rho_m(\boldsymbol{r})\rho_{m'}(\boldsymbol{r}')$. By considering only the leading linear order of the dependence, we have the following expression for the surface energy:

$$J(\rho_m(\boldsymbol{r}),\rho_{m'}(\boldsymbol{r}'))=\eta_{\rm CC}-\nu\frac{\rho_m(\boldsymbol{r})\rho_{m'}(\boldsymbol{r}')}{\rho_s^2}, \tag{10}$$

where a positively defined value $\eta_{\rm CC}$ represents the strength of the surface energy between cells, which is independent of $\rho_m(\boldsymbol{r})$; a positively defined value ν represents the surface energy gain for cell-cell adhesion; and ρ_s is the saturation concentration for the adhesion molecule. For simplicity, we assume that these values are independent of the cell index m.

The intuitive meaning of Eq. (10) is as follows: By the negative sign for the second term in Eq. (10), the equation expresses the fact that the presence of concentration product $\rho_m(\boldsymbol{r})\rho_{m'}(\boldsymbol{r}')$ reduces the surface energy as shown in Fig. 3(b); that is, its presence stabilizes cell-cell contact. This represents the pair binding effect of the adhesion molecule, which stabilizes the cell-cell contact [14].

Next, we derive the polarization part of cell-cell adhesion on the basis of Eq. (10). We shall do this by expressing the spatial inhomogeneity in $\rho_m(\boldsymbol{r})$. For simplicity, we assume that $\rho_m(\boldsymbol{r})$ depends only on the direction from the center of the mth cell for the periphery site $\boldsymbol{r}$. The direction is denoted by $\boldsymbol{e}_m(\boldsymbol{r})$ as in Eq. (8). In this case, we can use the following multipole expansion (or the angular Fourier transform) [68]:

$$\rho_m(\boldsymbol{r})=\rho_s[\phi_0+\phi_1\boldsymbol{p}_m\cdot\boldsymbol{e}_m(\boldsymbol{r})+\cdots]. \tag{11}$$

Here, ϕ_0 is the constant magnitude of the unpolarized part of $\rho_m(\boldsymbol{r})$ shown in Fig. 3(c), ϕ_1 is the constant magnitude of the polarized part shown in Fig. 3(d), and $\boldsymbol{p}_m$ is a unit vector indicating the polarized direction of $\rho_m(\boldsymbol{r})$ as shown in Fig. 3(d). $\boldsymbol{p}_m$ is the degree of freedom obeying the constitutive equation given later. The motion of $\boldsymbol{p}_m$ through the constitutive

equation gives a coarse-grained expression of the dynamics of $\rho_m(\boldsymbol{r})$.

For simplicity, we assume that ϕ_0 and ϕ_1 do not depend on the cell index m. We consider only the front-side polarization in the concentrations and, to express this, we ignore the higher oscillatory terms denoted by "..." in Eq. (11). We also impose the positivity of the concentration $\rho_m(\boldsymbol{r})$ and $\max\rho_m(\boldsymbol{r}) = \rho_s$ to determine ϕ_0 and ϕ_1.

By the substitution of the expression in Eq. (11) for $\rho_m(\boldsymbol{r})$ in Eq. (10), $J_{m(\boldsymbol{r})m(\boldsymbol{r}')}$ reads

$$J(\rho_m(\boldsymbol{r}),\rho_{m'}(\boldsymbol{r}')) = J_{CC} - \frac{J_A}{4}[1+\theta\,\boldsymbol{p}_m\cdot\boldsymbol{e}_m(\boldsymbol{r})] \times[1+\theta\,\boldsymbol{p}_{m'}\cdot\boldsymbol{e}_{m'}(\boldsymbol{r}')], \tag{12}$$

where $J_{CC} = \eta_{CC} + \nu$ is the basal adhesion that represents the unpolarized part of the cell-cell adhesion, $J_A = 4\nu\phi_0^2$ is the polarized part, and $\theta = \phi_1/\phi_0$. As the strength of the cell-cell adhesion, we use Eq. (12) to express the polarized cell-cell adhesion.

Here, let us quote similar previous works relating to polarized cell-cell adhesion [61,62] in order to clarify the differences of the formulation of adhesion in Eq. (12) from that in previous work. In these previous works, a polarization in the cell-cell adhesion for a biaxial anisotropy was introduced into $J_{mm'}$ in a heuristic way [61,62]. The polarization successfully reproduces the convergent extension during the development of *Xenopus* and *Drosophila*. In these cases, the regions of high adhesion molecule concentration exist on two opposite sides of the cell. Thus, the scenario for *Xenopus* and *Drosophila* differs from that for Dd because the polarized cell-cell adhesion of Dd has only a single high concentration region, and it lies on the front side of the cell as shown in Fig. 1(a). The situation in the cases of *Xenopus* and *Drosophila* is intuitively expected to trivially reproduce a side-by-side contact when regions of high concentration lie on the two lateral sides of the cell. However, this mechanism of side-by-side contact is not equivalent to that in the case of Dd. Therefore, we needed the formulation in Eq. (12) to express the polarized cell-cell adhesion in Dd.

Finally, we consider the equation of motion for $\boldsymbol{p}_m$. As mentioned above, this paper aims to clarify the effects of cell-cell adhesion polarized in the front side of the cell as shown in Fig. 3(a). For this purpose, we consider the simplest constitutive equation,

$$\boldsymbol{p}_m = \boldsymbol{\mu}_m. \tag{13}$$

Hence, we identify the dynamics of $\boldsymbol{\mu}_m$ as that of $\boldsymbol{p}_m$.

Here, we emphasize the difference between the constitutive equation (13) for $\boldsymbol{p}_m$ and that in previous works [61,62]. In the previous works, the polarization in the adhesion is aligned with the direction of the cell's elongation; the alignment feature is not equivalent to cell motility. In contrast, Eq. (13) directly couples the polarization in cell-cell adhesion, $\boldsymbol{p}_m$, with the self-propulsion direction $\boldsymbol{\mu}_m$, which is strongly related to cell motility.

C. Dynamics of cell polarities

The self-propulsion of a cell in our model is formulated by using Eq. (6). Equation (6) contains the cell polarity $\boldsymbol{\mu}_m$, which is a degree of freedom. In this subsection, we formulate the equation of motion for $\boldsymbol{\mu}_m$. As is well known, Dd exhibits a persistent random walk [69,70], where the direction of the cell's motion is maintained for a duration τ. To reproduce this walk, a normalized mean velocity over τ is conventionally employed for $\boldsymbol{\mu}_m$ [7,20,58]. A possible realization of the mean velocity expression is

$$\boldsymbol{\mu}_m \propto \int_{-\infty}^{t} dt'\chi(d\boldsymbol{R}_m/dt')\exp[(t'-t)/\tau]/\tau a, \tag{14}$$

where $d\boldsymbol{R}_m/dt$ is the derivative of $\boldsymbol{R}_m$ in Eq. (7) with respect to time t, the unit of time t is set to a single Monte Carlo step, χ is the ratio of the change in $\boldsymbol{\mu}_m$ to the change in $d\boldsymbol{R}_m/dt$, and a is the lattice constant.

When the equation of motion (14) is solved numerically, a history of the $d\boldsymbol{R}_m/dt$ must be kept. By using the corresponding differential formula, however, one can reduce the memory requirement. By the differentiation of Eq. (14), we obtain the differential formula,

$$\frac{d\boldsymbol{\mu}_m}{dt} \propto \frac{1}{\tau}\left[\frac{\chi}{a}\frac{d\boldsymbol{R}_m}{dt} - \boldsymbol{\mu}_m\right]. \tag{15}$$

This formula produces a change in the norm of $\boldsymbol{\mu}_m$ as time advances; this is contradictory to the definition of the unit vector $\boldsymbol{\mu}_m$. One can solve this issue by setting the part parallel to $\boldsymbol{\mu}_m$ in the right side of Eq. (15) to zero. To do this, we subtract $\boldsymbol{\mu}_m(\chi d\boldsymbol{R}_m/adt\cdot\boldsymbol{\mu}_m - 1)/\tau$ from the right side of Eq. (15), and then we have

$$\frac{d\boldsymbol{\mu}_m}{dt} = \frac{\chi}{\tau a}\frac{d\boldsymbol{R}_m}{dt} - \frac{\chi}{\tau a}\left(\frac{d\boldsymbol{R}_m}{dt}\cdot\boldsymbol{\mu}_m\right)\boldsymbol{\mu}_m. \tag{16}$$

In the present work, we use this equation of motion for $\boldsymbol{\mu}_m$. Note that this equation is essentially equivalent to the corresponding equation used previously [71].

For ease of integrating Eq. (16) in the present simulation, the adiabatic approximation is assumed as follows: Eq. (16) is integrated numerically by the Euler method in the polar coordinate expression corresponding to $\boldsymbol{\mu}_m$. The integration is carried out only between two consecutive Monte Carlo steps. This approximation is based on the assumption that $\boldsymbol{\mu}_m$ varies very slowly during a single Monte Carlo step. This approximation means that $\boldsymbol{\mu}_m$ is adiabatically decoupled from the copy process for Potts states in the Monte Carlo step. That is to say, all changes in $m(\boldsymbol{r})$ in a single Monte Carlo step occur simultaneously in the time scale of the change in $\boldsymbol{\mu}_m$. Since the time scale of $\boldsymbol{\mu}_m$ is τ/χ, this approximation is justified for large values of τ/χ.

For the integration of Eq. (16), $d\boldsymbol{\mu}_m/dt$ strongly depends on the timing of $\boldsymbol{R}_m$ used in the equation. To determine the timing, we further introduce the approximation that the time scale of the change in $\boldsymbol{R}_m$ is of the same order as that of $\boldsymbol{\mu}_m$. For consistency between these time scales, we assume that χ is of the order of unity. Furthermore, $\boldsymbol{R}_m$ is assumed to be constant during the Monte Carlo step. Hence, $\boldsymbol{R}_m$ is calculated only once [using Eq. (7)] for each Monte Carlo step. We carry out this calculation before the numerical integration of Eq. (16).

III. NUMERICAL SIMULATION

A. Simulation conditions

Since the present paper addresses collective cell migration, we start our study from its realization in our model. For this purpose, we need to specify the strength of the polarized cell-cell adhesion J_A, which effects the collective cell migration. To specify the strength, we carry out a search for suitable parameter values, examining steady states for criteria for collective cell migration. As criteria, we adopt a simple definition of collective cell migration from Ref. [39] for convenience. The definition consists of the following two conditions: The first condition is the existence of mechanical cell-cell contacts. In our model, mechanical contact simply corresponds to contact between cells. The second condition is the presence of supracellular polarity and cytoskeleton organization. In our model, the supracellular polarity corresponds to the intercellular order in the cell polarity $\boldsymbol{\mu}_m$. In our search for parameter values, we utilize these two conditions as an indicator of collective cell migration.

In this subsection, we determine the other simulation parameters used in this parameter value search. To reduce calculation costs in this determination, we specify the typical steady state of $J_A = 0$ and determine the corresponding typical parameters. These typical parameters are used in the parameter value search described in the subsections that follow.

Let us begin by determining the size parameters for this simulation and the boundary condition. The size of the simulation needs to be determined in order to control the calculation cost. Since the calculation cost strongly depends on cell density, an appropriate condition for cell density should be clarified. Therefore, we discuss the appropriate condition for cell density. In the present work, we have an interest in a nontrivial cell-alignment pattern in a steady state. Therefore, low cell densities are preferable to avoid highly confluent states having only trivial cell alignments, such as simple aggregation. In contrast, to reduce the calculation cost of the steady state, high cell densities are preferable; this is because the relaxation time for cell-cell contact increases as cell density decreases, giving rise to a larger calculation cost. To satisfy these two opposing conditions, adequate cell densities are the most preferable.

In order to establish a value for adequate cell density, we choose the size parameters for the simulation: the number of cells, $N_{\mathrm{Cell}} = 256$; the maintenance target for the cell volume, $V = 64$; and the system size, $L = 196$. Since the corresponding volume fraction $N_{\mathrm{Cell}}V/L^2 \sim 43\%$, highly confluent states covering the whole system are avoidable. In our observation, the cell density relaxes quickly to a steady-state number of cell-cell contacts. The typical relaxation time scale is of the order of 10^4 Monte Carlo steps at most for typical parameters of our simulation. To obtain the steady state, we employ 10^5 Monte Carlo steps and then 5×10^4 Monte Carlo steps to average observables. These periods are much longer than the relaxation time and therefore allow a steady state to be reached. When we use parameter values that give rise to much longer relaxation times, we note these exceptions in the text.

As the boundary condition of the system, we use a periodic boundary condition so that the cells can move freely through the boundary. This type of boundary condition is useful to avoid the suppression of collective cell migration via the collision of cells with the boundary.

Next, we determine the parameter values for the unpolarized part of cell-cell adhesion. In the unpolarized part, the ratio of the adhesion to the periphery tension, J_{CC}/J_{CE}, is the main determinant of the steady state. Conventionally, instead of this ratio, Glazier and Graner's surface tension [64,65],

$$\gamma = 1 - \frac{1}{2}\frac{J_{CC}}{J_{CE}}, \tag{17}$$

is used as a control parameter. Here, we normalize the γ previously given by J_{CE} to simplify the expression. Since the unpolarized part strongly affects the steady state of mechanical cell-cell contact, we determine the typical γ for reaching typical steady states of mechanical contacts.

To determine this value, we revisit these steady states, which have been well studied previously for the unpolarized case ($J_A = 0$) [33,64,65]. At the zero-temperature limit, cells contact each other when $\gamma > 0$ and do not make contact when $\gamma < 0$. At finite temperatures, the steady states are as shown in Figs. 4(a)–4(f). Here, we set $J_{CE} = 2$ and consider three values of γ. For $\gamma = 0.25$ ($J_{CC} = 3$), the snapshots are shown in Figs. 4(a) and 4(d); the figures show that cells isotropically form contacts with each other and form aggregations. For $\gamma = 0$ ($J_{CC} = 4$), isotropic contacts seem to be almost stable and are only slightly destabilized as shown in Figs. 4(b) and 4(e). For $\gamma = -0.25$ ($J_{CC} = 5$), cells disperse and have almost no contact with other cells, as shown in Figs. 4(c) and 4(f), except for incidental unstable contacts due to the high cell density.

From these results, it is concluded that, at very near $\gamma = 0$, the cells switch between contacted and uncontacted states. These two states are the known typical states for mechanical cell-cell contact for unpolarized cell-cell adhesion ($J_A = 0$). We hereinafter employ these three values of γ for the parameter value search.

Lastly, we determine the values for parameters related to cell motility. The constants for the volume stiffness κ and self-propulsion E are unity in the present simulation; these settings establish a condition in which cells easily move by their deformation. We additionally employ $\tau a/\chi = 10$. Our simulation result does not crucially depend on this value, excluding extremely small values where the discretization of Eq. (16) induces a numerical instability.

The inverse temperature β also significantly affects cell motility [64]. To obtain highly mobile cells, which mimic starved Dd, we should use a low β. Therefore, we employ values of β equal to or less than unity in order to incorporate high cell motility. However, as is already known, a β value that is too low gives rise to the unrealistic destruction of the cell. To obtain a sufficiently low value of β to allow highly mobile cells to be stably simulated, we check the dependence of steady states on β. For $\beta = 0.1$, a roughness in the cell periphery appears as shown in Figs. 4(a)–4(c); in this case, the cells are partially destroyed. To reduce this destruction of cells, we employ values of β greater than or equal to 0.1.

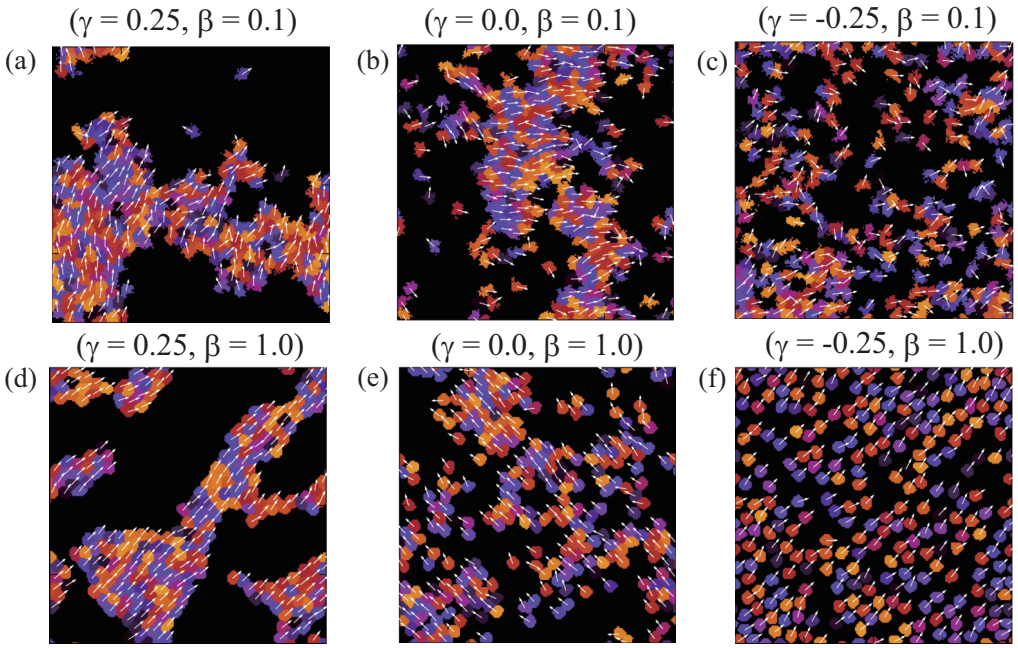

FIG. 4. Snapshots of steady states for (a) $\gamma = 0.25$ and $\beta = 0.1$, (b) $\gamma = 0$ and $\beta = 0.1$, (c) $\gamma = -0.25$ and $\beta = 0.1$, (d) $\gamma = 0.25$ and $\beta = 1.0$, (e) $\gamma = 0$ and $\beta = 1.0$, and (f) $\gamma = -0.25$ and $\beta = 1.0$. Other parameters are given in the main text. Black regions represent empty spaces, and other colored regions represent cells, with different colors representing different cells. The white arrow at each cell's center indicates the direction of $\boldsymbol{\mu}_m$.

B. Mechanical cell-cell contact

From here, we move on to the confirmation of collective migration of cells with polarized cell-cell adhesion ($J_A > 0$). In this subsection, we quantitatively examine the existence of mechanical cell-cell contacts, which is the first condition of collective cell migration. In particular, we clarify the J_A dependence of this existence. To quantitatively examine the existence of mechanical cell-cell contacts, we calculate a related value:

$$n_{CC} = \frac{1}{N_{Cell}} \sum_{\langle \boldsymbol{r}, \boldsymbol{r}' \rangle} \delta_{m(\boldsymbol{r})m(\boldsymbol{r}')}[1 - \delta_{m(\boldsymbol{r})0}][1 - \delta_{0m(\boldsymbol{r}')}]. \quad (18)$$

On the right side, $\delta_{m(\boldsymbol{r})m(\boldsymbol{r}')}$ restricts the adjacent sites to those that are occupied by different cells or by both a cell and the empty space. In addition, $1 - \delta_{m(\boldsymbol{r})0}$ excludes the latter case. Hence, n_{CC} is the total number of site pairs that represent cell-cell contacts. Therefore, n_{CC} is available as a probe for the existence of mechanical cell-cell contacts.

To calculate the J_A dependence of n_{CC}, we carry out simulations for values of J_A from 0 to 4.0 for the cases of $\gamma = -0.25$ and $\gamma = 0$. For the case of $\gamma = 0.25$, we consider J_A from 0 to 3.0 because the cell is unstable at $J_A \geqslant 3.0$. We start the simulations at $J_A = 0.0$. As the initial state of $\{m(\boldsymbol{r})\}$ for $J_A = 0$, we choose a square lattice array of cells without cell-cell contacts. For the initial state of $\boldsymbol{\mu}_m$, we choose a random alignment. To obtain a steady state, we perform a relaxation simulation for 10^5 Monte Carlo steps. Then, we calculate the time-averaged value of n_{CC} during 5×10^4 Monte Carlo steps. After the completion of the time-average calculation, we increase J_A by the incremental value of 0.2 and repeat the same procedure for the case of $J_A = 0.2$. The same procedure is repeated for incrementally larger values of J_A up to the upper bound.

In this simulation, we employ the largest value of θ in Eq. (12), namely $\theta = 1$. This choice of θ aims to maximize the effect of polarized cell-cell adhesion so that it can be easily observed. This may lead to an overestimation of the effect. However, the choice is effective in the present situation in that we lack quantitative data about polarization in the actual system.

The calculated n_{CC} values are plotted in Figs. 5(a)–5(c). For the case of $\gamma = 0.25$, shown in Fig. 5(a), n_{CC} takes large values, ranging from 80 to 100. The values are more than twice the perimeters of the cells in our estimation, on which the number of periphery sites are about $2\pi r \simeq 30$ for a circular cell shape with cell volume $V = \pi r^2 = 64$. This large value reflects the fact that cells isotropically form cell-cell contacts and form a simple aggregation as shown in Figs. 4(a) and 4(d). n_{CC} values plotted for $\beta = 0.1$, 0.2, 0.3, 0.5, and 1.0 become slightly larger as β decreases. This is because the cell periphery becomes rougher as β decreases, and thereby the cell periphery available for cell-cell contact effectively elongates. n_{CC} also becomes slightly larger as J_A increases, simply because the increase in J_A promotes cell-cell contact. The dependencies of n_{CC} on these parameters are weak; this indicates that the aggregation is stable over changes of these parameters. Even for a γ value of 0, n_{CC} remains almost constant as shown in Fig. 5(b). In this case, cells are also expected to form cell-cell contacts almost isotropically.

When γ further decreases to $\gamma = -0.25$, n_{CC} values for small values of J_A are small in comparison with those at $\gamma = 0.25$ and $\gamma = 0$, as shown in Fig. 5(c). In particular, n_{CC} is close to 0 for high values of β, indicating an absence

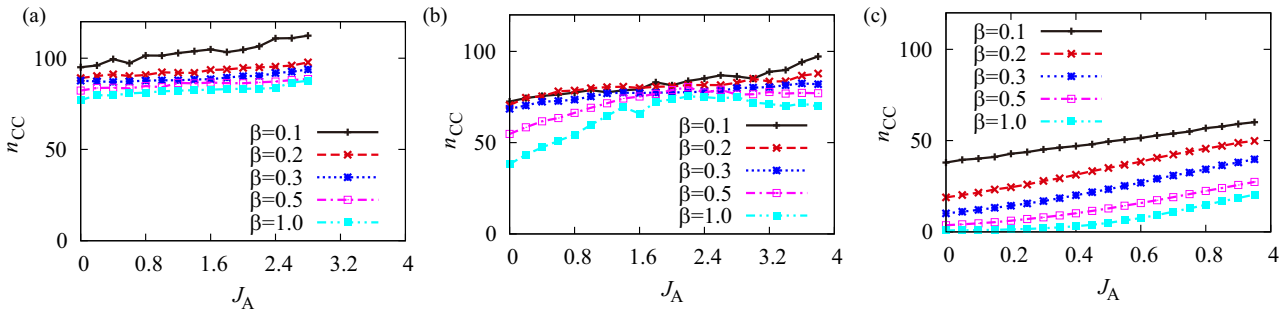

FIG. 5. Time-averaged n_{CC} as a function of J_A for (a) $\gamma = 0.25$, (b) $\gamma = 0$, and (c) $\gamma = -0.25$. The data are shown by a solid line for $\beta = 0.1$, a dashed line for $\beta = 0.2$, a dotted line for $\beta = 0.3$, a dashed-dotted line for $\beta = 0.5$, and a dashed-double-dotted line for $\beta = 1.0$. The other parameters are given in the main text. In (a), the data are not shown for $J_A > 3.0$ because the cells are unstable.

of cell-cell contacts in this case. Furthermore, in contrast to $\gamma = 0$, at $\gamma = -0.25$, n_{CC} takes values only up to 60 even when J_A increases to 4.0. In this case, the result implies the possibility that cells form partial contacts with other cells. A partial contact is expected to reflect a nontrivial style of cell-cell contact. The contacts may stabilize a cell alignment, which is not shown in Figs. 4(a)–4(f).

In summary, mechanical cell-cell contacts exist except in the case of negative γ, high β, and small J_A. In particular, only in the case of negative γ and large J_A do we find partial contact. In this case, we expect a characteristic style of cell-cell contact induced mainly by the polarization part of cell-cell adhesion. This is reasonable because the unpolarized part does not contribute to the stabilization of cell-cell contacts for negative values of γ. We also expect that high β is preferable for observing the characteristic style of cell-cell contact because the styles of partial contact become unclear owing to the roughening of the cell periphery at low values of β. Therefore, with regard to the aspect of mechanical cell-cell contact, the parameter values of negative γ, high β, and large J_A provide a good candidate case for cells to form a characteristic style of cell-cell contact induced by polarized cell-cell adhesion.

C. Supracellular polarity

In this subsection, we proceed to the examination of the second condition of collective cell migration. This condition is the formation of supracellular polarity and cytoskeleton organization. In the present model, supracellular polarity corresponds to the multicellular order of cell polarity $\boldsymbol{\mu}_m$. To quantitatively examine this order, we define an order parameter for cell polarity M by

$$M = \frac{1}{N_{\mathrm{Cell}}} \left| \sum_{m=1}^{N_{\mathrm{Cell}}} \boldsymbol{\mu}_m \right|. \tag{19}$$

In a perfectly polarity-ordered state, where all $\boldsymbol{\mu}_m$'s align in the same direction, M is unity. In the disordered state of $\boldsymbol{\mu}_m$, M is small. Therefore, M is useful as a probe for the multicellular order of $\boldsymbol{\mu}_m$. We calculate the J_A dependence of M to obtain adequate values of J_A for realizing collective cell migration.

The calculated M values are plotted in Figs. 6(a)–6(c) for the same conditions as were used for the calculation of n_{CC}. M takes values larger than 0.5 and is almost independent of γ, β, and J_A. This result shows that a multicellular order of $\boldsymbol{\mu}_m$ appears for any parameter values used in our simulations. Therefore, the second condition of collective cell migration will usually be satisfied in the parameter ranges used in our simulation.

Note that multicellular order exists even in the case without cell-cell contacts. This is already known to be a common feature for self-propelled particles with steric interactions [72–75], a deformable shape [44,76], or an elastic core [77].

To obtain further insights into the steady state of $\boldsymbol{\mu}_m$, we investigate the spatial fluctuation of $\boldsymbol{\mu}_m$. With this multicellular order, fluctuations in $\boldsymbol{\mu}_m$ are expected to be suppressed. The suppression is seen in the correlation function of $\boldsymbol{\mu}_m$ as a rapid decay [78–80]. To check this expectation, we consider the

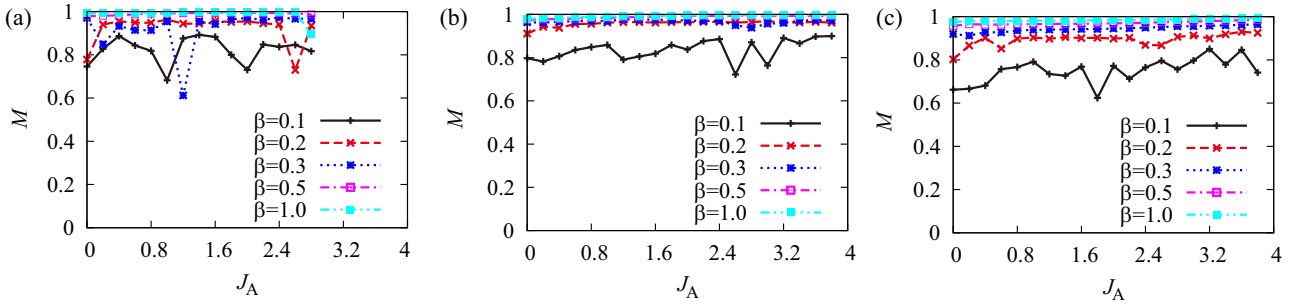

FIG. 6. The time-averaged order parameter M as a function of J_A for (a) $\gamma = 0.25$, (b) $\gamma = 0$, and (c) $\gamma = -0.25$. The data are shown by a solid line for $\beta = 0.1$, a dashed line for $\beta = 0.2$, a dotted line for $\beta = 0.3$, a dashed-dotted line for $\beta = 0.5$, and a dashed-double-dotted line for $\beta = 1.0$. The other parameters are given in the main text. In (a), the data are not shown for $J_A > 3.0$ because the cells are unstable.

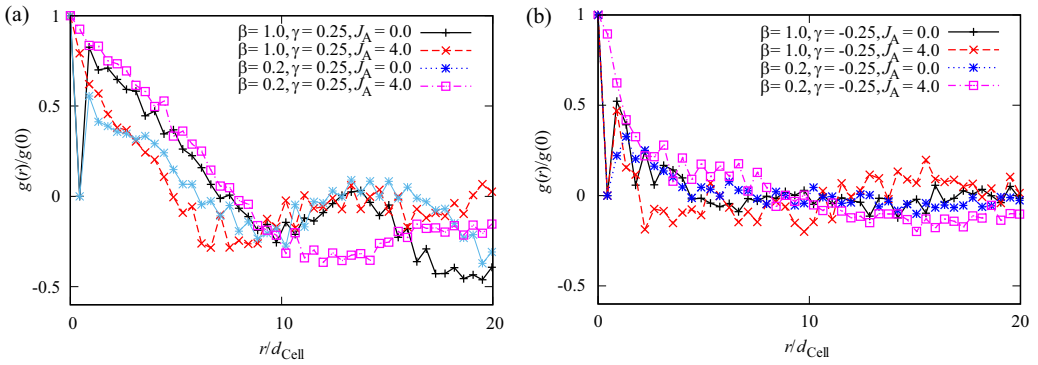

FIG. 7. The correlation function $g(r)/g(0)$ for $\boldsymbol{\mu}_m$, for (a) $\gamma = 0.25$ and (b) $\gamma = -0.25$. In both panels, the solid, dashed, dotted, and dashed-dotted lines represent $g(r)/g(0)$ for $\beta = 1.0$ and $J_A = 0.0$, for $\beta = 1.0$ and $J_A = 4.0$, for $\beta = 0.2$ and $J_A = 0.0$, and for $\beta = 0.2$ and $J_A = 4.0$, respectively. The other parameters are given in the main text. d_{Cell} represents the average cell diameter $\sqrt{V/\pi} \simeq 9.02a$.

correlation function

$$g(r) = \frac{1}{N(r)} \sum_{\langle m,n \rangle} \boldsymbol{\mu}_m \cdot \boldsymbol{\mu}_n \delta(|\boldsymbol{R}_m - \boldsymbol{R}_n| - r) - M^2. \quad (20)$$

Here, $\langle m,n \rangle$ indicates the summation over all cell pairs, and $N(r)$ represents the number of cell pairs having an intrapair distance of r. The calculated correlation function values are shown in Figs. 7(a) and 7(b). As expected, the correlation function decays at around ten cells for $\gamma = 0.25$ and at a few cells for $\gamma = -0.25$. The decay in these curves is almost independent of β and J_A. This indicates that the formation of multicellular order is independent of the parameters.

By combining these observations with the results in the previous subsection, we conclude that both conditions of collective cell migration are satisfied, except in the cases of $\gamma = -0.25$, low β, and small J_A, at which mechanical contacts are not formed. From these results, we can successfully specify J_A for observing collective cell migration. In particular, we previously suggested that cases with negative γ, high β, and large J_A are candidates for cells to exhibit a characteristic style of cell-cell contact induced by polarized cell-cell adhesion. In the next subsection, we concentrate on these cases and examine them for the characteristic style of cell-cell contact.

D. Contact due to polarized adhesion

Finally, we examine the characteristic style of cell-cell contact by polarized cell-cell adhesion. In particular, we attempt to show that the style is side-by-side contact resulting from the synergy between polarized cell-cell adhesion and cell motility. This style is expected only for negative γ and high β as discussed previously. Therefore, we employ $\gamma = -0.25$ and $\beta = 1.0$. The other model parameters are the same as those given in the previous subsection.

Our main purpose is to examine whether polarized cell-cell adhesion induces side-by-side contact, as is suggested experimentally [26,30]. Therefore, we examine the possibility of side-by-side contact. To do this, we define the following quantity related to lateral contact:

$$n_L = \frac{1}{N_{Cell}} \sum_{\langle \boldsymbol{r},\boldsymbol{r}' \rangle} \delta_{m(\boldsymbol{r})m(\boldsymbol{r}')}[1 - \delta_{m(\boldsymbol{r})0}] \times [1 - \delta_{0m(\boldsymbol{r}')}] w(m(\boldsymbol{r}),\boldsymbol{r}) w(m(\boldsymbol{r}'),\boldsymbol{r}'), \quad (21)$$

$$w(m,\boldsymbol{r}) = 1 - [\boldsymbol{e}_m(\boldsymbol{r}) \cdot \boldsymbol{\mu}_m]^2. \quad (22)$$

Lateral contact is defined as cell-cell contact perpendicular to the cell polarity $\boldsymbol{\mu}_m$. The quantity n_L is the total number of site pairs having cell-cell contacts, weighted by $w(m,\boldsymbol{r})$. Since the side-by-side contact shown in Fig. 1(c) has a larger value of $w(m,\boldsymbol{r})$ than other styles of contacts, this weight is useful for eliminating the contribution of other styles of cell-cell contact. As a result of this elimination, n_L is available as a probe for the formation of side-by-side contacts.

In this examination, we calculate the dependence of n_L on J_A in order to learn the effect of the polarized part of cell-cell adhesion. For J_A, we sweep its value in the same way as in the previous subsections. In addition, we carry out a comparison of the frequency of side-by-side contacts with the frequency of other styles of contact in order to effectively evaluate the predominance of side-by-side contact. To do this, we also calculate $n_{NL} = n_{CC} - n_L$. These values are averaged over 5×10^4 Monte Carlo steps and plotted in Fig. 8. For small J_A, both n_L and n_{NL} take similar small values. As J_A increases up to 1, their values remain small. Then, as J_A further increases, n_L increases more rapidly than n_{NL}. In the inset, the fractions

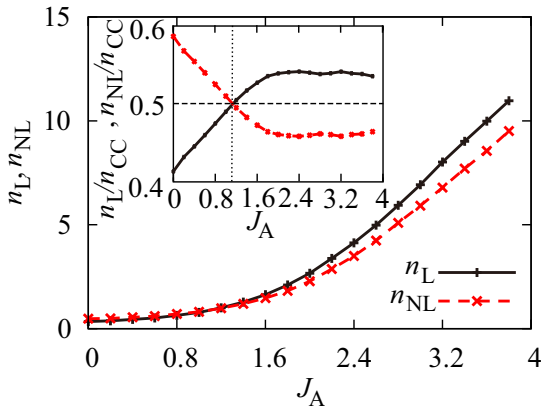

FIG. 8. The number of lateral contacts n_L (solid line and "+" markers) and the number of nonlateral contacts n_{NL} (dashed line and "×" markers) as a function of J_A. The data are calculated for $\beta = 1.0$ and $\gamma = -0.25$. The other parameters are given in the main text. The inset shows the relative proportions of n_L and n_{NL}.

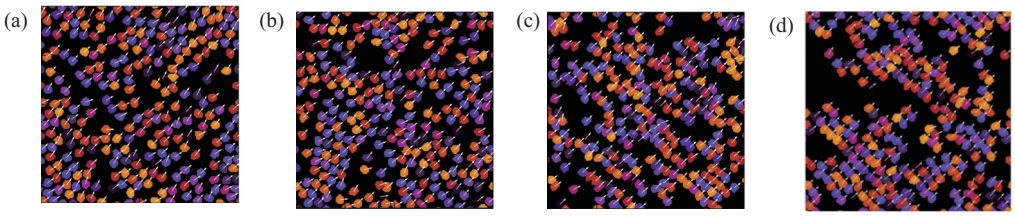

FIG. 9. Snapshots of steady states for (a) $J_A = 0$, (b) $J_A = 0.5$, (c) $J_A = 1.0$, and (d) $J_A = 4.0$. Other parameters are given in the main text. The black region represents $m = 0$, and other colored regions represent cells, with different colors representing different cells. The white arrow at each cell's center indicates the direction of $\boldsymbol{\mu}_m$.

n_L/n_{CC} and n_{NL}/n_{CC} are shown. For small J_A, n_L/n_{CC} is smaller than n_{NL}/n_{CC}. As J_A increases, n_L/n_{CC} increases and becomes larger than n_{NL}/n_{CC} for $J_A \gtrsim 1$. This indicates that the polarized part of cell-cell adhesion promotes the formation of side-by-side contact.

Note that the increase in n_L with increasing J_A is gradual. Thus, there is no phase transition from the state of uncontacted cells to the state with side-by-side contacts; the transition between the two states occurs as a crossover. This contrasts with the discontinuous transition between the contacted state and the uncontacted state around $\gamma \simeq 0$. The difference may reflect the one-dimensional characteristics of cell alignment through side-by-side contacts. That is, when cells align in only one dimension, no long-range order in finite temperatures is expected from the low dimensionality [81,82], and, therefore, no phase transition is expected.

To directly confirm the formation of one-dimensional cell alignment with side-by-side contact, we show snapshots of the configurations in Figs. 9(a)–9(d). As shown in Figs. 9(a) and 9(b), respectively, almost no cell-cell contacts for $J_A = 0$ or $J_A = 0.5$ are observed. In contrast with these cases, in the case of $J_A = 1.0$, shown in Fig. 9(c), cells align in the direction perpendicular to their cell polarity and form side-by-side contacts. The side-by-side contacts are observed up to $J_A = 4.0$ as shown in Fig. 9(d). Furthermore, as expected from the above, cells clearly form a one-dimensional short lateral array with increasing J_A.

Up to this point, we have focused only on the effect of polarized cell-cell adhesion on the formation of side-by-side contact. In order to show that contact formation is a synergetic effect between cell motility and polarized cell-cell adhesion, we now go on to focus on cell motility. To examine the effect of cell motility, we calculate n_L and n_{NL} as a function of E.

Before performing this calculation, we need to consider the difficulty of simulation for small E. In the case of $E = 1$, n_L and n_{NL} rapidly relax, with a typical relaxation time scale [33]. Unfortunately, the transition from relaxation to the steady state is very slow for $E \simeq 0$ because of a power law relaxation in the Lifshitz-Slyozov growth of cell aggregation [83]. Therefore, a systematic calculation of small values of E is difficult to carry out. In fact, n_L and n_{NL} for the same parameters with $E \simeq 0$ do not relax in our calculation time. To overcome this difficulty, we use $\beta = 0.5$ to boost the relaxation. As a side effect of this boosting, the decreasing of β from 1.0 to 0.5 makes it difficult to visually distinguish the side-by-side contact from other styles. To solve this issue, we employ the relative proportions of n_L and n_{NL} in n_{CC} as a probe for the effect of E. In addition, to enhance the detectability of the effect of E, we use $J_A = 4.0$, which readily induces side-by-side contact.

We calculate the dependence of n_L and n_{NL} on E by a series of simulations while sweeping through values of J_A, as in previous subsections. Here, we use an incremental value of 0.04 for increasing E and set an upper bound of 1.0. The calculation result as a function of E is shown in Fig. 10. For small values of E, cells may not sufficiently relax to a steady state because of the reason discussed above. However, they form small clusters like those in Fig. 4(c), and, thereby, n_L and n_{NL} relax to a value comparable to those for large values of E. The relative proportions are shown in the inset. The proportion of n_L increases in comparison with that for n_{NL}; this suggests that cell motility promotes the formation of side-by-side contact. This result implies a synergy between polarized cell-cell adhesion and cell motility in side-by-side contact formation.

IV. SUMMARY AND DISCUSSION

In the present paper, we have examined theoretically the formation of side-by-side contact by cells with polarized cell-cell adhesion in collective cell migration. We constructed a model expressing polarized cell-cell adhesion on the basis of the cellular Potts model and carried out numerical simulations of collective cell migration. We have demonstrated the formation of lateral arrays of cells with side-by-side contacts in a certain

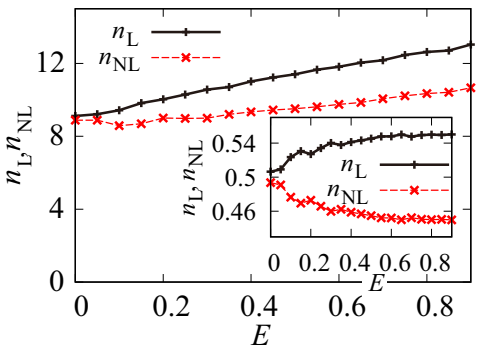

FIG. 10. The number of lateral contacts n_L (solid line and "+" markers) and the number of nonlateral contacts n_{NL} (dashed line and "×" markers) as a function of E. The data are calculated for $\beta = 0.5$ and $\gamma = -0.25$. The other parameters are given in the main text. The inset shows the relative proportions of n_L and n_{NL}.

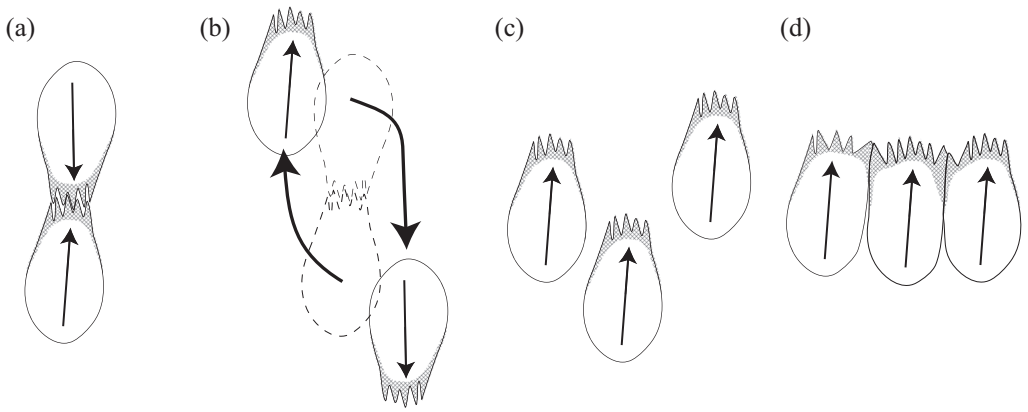

FIG. 11. Schematic images to explain side-by-side contact formation. The arrows in the cells represent cell polarity. Darkened areas indicate regions with high concentrations of cell-cell adhesion molecules. The sawtooth shape at the front of the cell indicates pseudopods. (a) Cells with front-to-front contact. (b) Cells whose front-to-front contact is destabilized by the motility of the cells. (c) Cells whose cell polarity and direction of movement are aligned in the same direction. (d) Cells that make side-by-side contact at their fronts.

case even though the intuitive expectation is that polarized cell-cell adhesion would induce front-to-front contacts of cells as shown in Fig. 1(c).

Let us discuss the mechanism of side-by-side contact formation. We propose that this side-by-side contact formation essentially results from a synergy between cell motility and polarized cell-cell adhesion as follows: If front-to-front contact were stable as expected, side-by-side contact would not occur. In reality, however, front-to-front contact is unstable in the case of a highly mobile cell. To demonstrate this instability, we consider the front-to-front contact of two cells as shown in Fig. 11(a). As expected, if the cell motility is strong enough to break the adhesion contact between the cells, the motion of the two cells destabilizes the front-to-front contact by making the cells move in opposite directions, as shown in Fig. 11(b). In addition, by analogy with the results of self-propelled particles [74,75], the cells are expected to align according to the direction of their motion as shown in Fig. 11(c). In this alignment, polarized cell-cell adhesion stabilizes the side-by-side contact near the front side of the cell as shown in Fig. 11(d), and hence the lateral alignment appears. As a result, the cells form the side-by-side contact shown in Fig. 9(c).

Side-by-side contact is also observed in experiments [26,30]. This side-by-side contact is an observation intuitively peculiar to the case of front-side polarized cell-cell adhesion [19]. Contrary to the intuitive expectation, our result supports the counterintuitive observation on the basis of the front-side polarization. Therefore, this work may bridge the gap between the polarization in the cell-cell adhesion and the cell alignment that are independently observed in the two different experiments.

We should note that our setting does not agree perfectly with the scenario in the above experiment in which side-by-side contacts were observed. In that experiment, cells exhibited aggregation by chemotaxis [26,30]. Since chemotaxis is not considered in the present paper, cell migration in our model does not rigorously express the effects of chemotaxis in the corresponding experiments. However, if we assume that the chemotaxis effect only caused cells to be attracted to each other and thereby made them condense, the condensation is also realized artificially in our simulation; that is, the effect of the chemotaxis is eventually realized in our simulation by our choice of model parameter values. In this case, our result gives a candidate mechanism for the experimental observation on the basis of the polarized cell-cell adhesion.

As for side-by-side contact, a quantitative analysis based on experimental data is currently lacking. To clarify the effect of polarized cell-cell adhesion, a comparison of the result of this simulation with experimental results would be meaningful. For this purpose, an experiment without chemotaxis effects would be preferable in order to examine the effects of pure polarized cell-cell adhesion separately from the effects of chemotaxis. To close this paper, we suggest the possibility that such an experiment could make use of the kinase-inactive (KI) mutant of Dd [84,85]. Using this mutant, it is possible to perform experiments at high concentrations of cells without the involvement of chemotaxis effects [86]. Thus, if conditions for cells in the early streaming stage are realized in the future, it may make possible a quantitative experimental comparison with this work.

ACKNOWLEDGMENTS

This work was supported by JSPS KAKENHI Grant No. 15K17740. The author would like to thank M. Kikuchi, K. Nemoto, R. Ishiwata, H. Kuwayama, N. Nakamura, K.-i. Hironaka, D. Mashiko, and T. Oura for having meaningful discussions. The author also thanks K. Fujimoto and H. Yoshino for their generous support.

[1] C. J. Weijer, J. Cell Sci. **122**, 3215 (2015).
[2] P. Friedl and D. Gilmour, Nat. Rev. Mol. Cell Biol. **10**, 445 (2009).
[3] P. Rørth, Annu. Rev. Cell Dev. Biol. **25**, 407 (2009).
[4] B. Szabó, G. J. Szollosi, B. Gonci, Z. Juranyi, D. Selmeczi, and T. Vicsek, Phys. Rev. E **74**, 061908 (2006).
[5] P. Lee and C. W. Wolgemuth, PloS Comput. Biol. **7**, e1002007 (2011).

[6] P. Lee and C. Wolgemuth, Phys. Rev. E **83**, 061920 (2011).
[7] A. J. Kabla, J. R. Soc. Interface **9**, 3268 (2012).
[8] T. Vicsek and A. Zafeiris, Phys. Rep. **517**, 71 (2012).
[9] M. C. Marchetti, J. F. Joanny, S. Ramaswamy, T. B. Liverpool, J. Prost, M. Rao, and R. A. Simha, Rev. Mod. Phys. **85**, 1143 (2013).
[10] E. Méhes and T. Vicsek, Comput. Adapt. Syst. Mod. **1**, 4 (2013).
[11] A. Haeger, K. Wolf, M. M. Zegers, and P. Friedl, Trends Cell Biol. **25**, 556 (2015).
[12] K. F. Swaney, C.-H. Huang, and P. N. Devreotes, Annu. Rev. Biophys. **39**, 265 (2010).
[13] T. J. Mitchison and L. P. Cramer, Cell **84**, 371 (1996).
[14] M. Takeichi, Nat. Rev. Mol. Cell. Biol. **15**, 397 (2014).
[15] U. S. Schwarz and S. A. Safran, Rev. Mod. Phys. **85**, 1327 (2013).
[16] C. Carmona-Fontaine, E. Theveneau, A. Tzekou, M. Tada, M. Woods, K. M. Page, M. Parsons, J. D. Lambris, and R. Mayor, Dev. Cell **21**, 1026 (2015).
[17] E. Méhes, E. Mones, V. Németh, and T. Vicsek, Plos One **7**, e31711 (2012).
[18] E. Theveneau and R. Mayor, Curr. Opin. Cell Biol. **24**, 677 (2012).
[19] J. C. Coates and A. J. Harwood, J. Cell Sci. **114**, 4349 (2001).
[20] W.-J. Rappel, A. Nicol, A. Sarkissian, H. Levine, and W. F. Loomis, Phys. Rev. Lett. **83**, 1247 (1999).
[21] A. Nicol, W. Rappel, H. Levine, and W. F. Loomis, J. Cell Sci. **112**, 3923 (1999).
[22] C.-H. Siu, T. J. Harris, J. Wang, and E. Wong, Semin. Cell Dev. Biol. **15**, 633 (2004).
[23] J. T. Bonner, *The Social Amoebae: The Biology of Cellular Slime Molds* (Princeton University Press, Princeton, 2009).
[24] D. A. Knecht, D. L. Fuller, and W. F. Loomis, Dev. Biol. **121**, 277 (2015).
[25] S. K. Brar and C.-H. Siu, J. Biol. Chem. **268**, 24902 (1993).
[26] K. Müller and G. Gerisch, Nature (London) **274**, 445 (1978).
[27] J. Faix, G. Gerisch, and A. A. Noegel, J. Cell Sci. **102**, 203 (1992).
[28] J. L. Dynes, A. M. Clark, G. Caulks, A. Cusp, W. F. Loomis, and R. A. Firtel, Genes Dev. **8**, 948 (1994).
[29] J. Wang, L. Hou, D. Awrey, W. F. Loomis, R. A. Firtel, and C.-H. Siu, Dev. Biol. **227**, 734 (2000).
[30] H. Beug, F. E. Katz, and G. Gerisch, J. Cell Biol. **56**, 647 (1973).
[31] H. Sesaki and C.-H. Siu, Develop. Biol. **177**, 504 (1996).
[32] F. Graner and J. A. Glazier, Phys. Rev. Lett. **69**, 2013 (1992).
[33] A. R. A. Anderson, P. M. A. J. Chaplain, and D. K. A. Rejniak, *Single-Cell-Based Models in Biology and Medicine* (Birkhauser Verlag AG, Basel, 2007).
[34] E. F. Keller and L. A. Segel, J. Theor. Biol. **26**, 399 (1970).
[35] E. F. Keller and L. A. Segel, J. Theor. Biol. **30**, 225 (1971).
[36] J. D. Murray, *Mathematical Biology II: Spatial Models and Biomedical Applications* (Springer, New York, 2003).
[37] J. A. Sherratt and J. D. Murray, Proc. R. Soc. London, Ser. B **241**, 29 (1990).
[38] M. H. Köpf and L. M. Pismen, Soft Matter **9**, 3727 (2013).
[39] M. H. Köpf, Phys. Rev. E **91**, 012712 (2015).
[40] D. Shao, W.-J. Rappel, and H. Levine, Phys. Rev. Lett. **105**, 108104 (2010).
[41] D. Shao, H. Levine, and W.-J. Rappel, Proc. Natl. Acad. Sci. USA **109**, 6851 (2012).
[42] G. R. Lázaro, A. Hernández-Machadoa, and I. Pagonabarraga, Soft Matter **10**, 7195 (2014).
[43] G. R. Lázaro, A. Hernández-Machadoa, and I. Pagonabarraga, Soft Matter **10**, 7207 (2014).
[44] J. Löber, F. Ziebert, and I. S. Aranson, Sci. Rep. **5**, 9172 (2015).
[45] S. Najem and M. Grant, Phys. Rev. E **93**, 052405 (2016).
[46] M. Basan, J. Elgeti, E. Hannezo, W.-J. Rappel, and H. Levine, Proc. Natl. Acad. Sci. USA **110**, 2452 (2013).
[47] N. Sepúlveda, L. Petitjean, O. Cochet, E. Grasland-Mongrain, P. Silberzan, and V. Hakim, PloS Comp. Biol. **9**, e1002944 (2013).
[48] B. A. Camley, J. Zimmermann, H. Levine, and W.-J. Rappel, Phys. Rev. Lett. **116**, 098101 (2016).
[49] J. Jeon, V. Quaranta, and P. T. Cummings, Biophys. J. **98**, 37 (2010).
[50] J. M. Osborne, A. Walter, S. K. Kershaw, G. R. Mirams, A. G. Fletcher, P. Pathmanathan, D. Gavaghan, O. E. Jensen, P. K. Maini, and H. M. Byrne, Philos. Trans. A. Math. Phys. Eng. Sci. **368**, 5013 (2010).
[51] S. T. Johnston, M. J. Simpson, and M. J. Plank, Phys. Rev. E **88**, 062720 (2013).
[52] B. Li and S. X. Sun, Biophys. J. **107**, 1532 (2014).
[53] C. Londono, M. J. Loureiro, B. Slater, P. B. Lücker, J. Soleasa, S. Sathananthan, J. S. Aitchison, A. J. Kabla, and A. P. McGuigan, Proc. Natl. Acad. Sci. USA **111**, 1807 (2014).
[54] K. Sato, T. Hiraiwa, and T. Shibata, Phys. Rev. Lett. **115**, 188102 (2015).
[55] K. Sato, T. Hiraiwa, E. Maekawa, A. Isomura, T. Shibata, and E. Kuranaga, Nat. Commun. **6**, 10074 (2015).
[56] A. F. M. Marée and P. Hogeweg, Proc. Natl. Am. Sci. USA **98**, 3879 (2001).
[57] V. A. Grieneisen, J. Xu, A. F. M. Marée, P. Hogeweg, and B. Scheres, Nature (London) **449**, 1008 (2007).
[58] J. B. Beltman, A. F. Marée, J. N. Lynch, M. J. Miller, and R. J. de Boer, J. Exp. Med. **204**, 771 (2007).
[59] R. M. Merks, S. V. Brodsky, M. S. Goligorksy, S. A. Newman, and J. A. Glazier, Dev. Biol. **289**, 44 (2006).
[60] A. Szabó and R. M. H. Merks, Front. Oncol. **3**, 87 (2013).
[61] M. Zajac, G. L. Jonesa, and J. A. Glazier, J. Theor. Biol. **222**, 247 (2002).
[62] R. M. A. Vroomans, P. Hogeweg, and K. H. W. J. ten Tusscher, PLoS Comput. Biol. **11**, e1004092 (2015).
[63] F.-Y. Wu, Rev. Mod. Phys. **54**, 235 (1982).
[64] J. A. Glazier and F. Graner, Phys. Rev. E **47**, 2128 (1993).
[65] F. Graner, J. Theor. Biol. **164**, 455 (1993).
[66] A. J. Ridley, M. A. Schwartz, K. Burridge, R. A. Firtel, M. H. Ginsberg, G. Borisy, J. T. Parsons, and A. R. Horwitz, Science **302**, 1704 (2003).
[67] R. Durrett and J. E. Steif, Ann. Probab. **21**, 232 (1993).
[68] E. Bertin, M. Droz, and G. Grégoire, Phys. Rev. E **74**, 022101 (2006).
[69] L. Li, S. F. Nørrelykke, and E. C. Cox, PLoS One **3**, e2093 (2008).
[70] H. Takagi, M. J. Sato, T. Yanagida, and M. Ueda, PLoS One **3**, e2648 (2008).
[71] A. Szabó, R. Ünnep, E. Méhes, W. O. Twal, W. S. Argraves, and Y. Cao, Phys. Biol. **7**, 046007 (2010).
[72] F. Peruani, A. Deutsch, and M. Bär, Phys. Rev. E **74**, 030904(R) (2006).
[73] A. Baskaran and M. C. Marchetti, Phys. Rev. Lett. **101**, 268101 (2008).

[74] J. Deseigne, O. Dauchot, and H. Chaté, Phys. Rev. Lett. **105**, 098001 (2010).
[75] C. A. Weber, T. Hanke, J. Deseigne, S. Leonard, O. Dauchot, E. Frey, and H. Chaté, Phys. Rev. Lett. **110**, 208001 (2013).
[76] A. M. Menzel and T. Ohta, Europhys. Lett. **99**, 58001 (2012).
[77] T. Hanke, C. A. Weber, and E. Frey, Phys. Rev. E **88**, 052309 (2013).
[78] L. Petitjean, M. Reffay, E. Grasland-Mongrain, M. Poujade, B. Ladoux, A. Buguin, and P. Silberzan, Biophys. J. **98**, 1790 (2010).
[79] T. E. Angelini, E. Hannezo, X. Trepat, J. J. Fredberg, and D. A. Weitz, Phys. Rev. Lett. **104**, 168104 (2010).
[80] D. T. Tambe, C. C. Hardin, T. E. Angelini, K. Rajendran, C. Y. Park, X. Serra-Picamal, E. H. Zhou, M. H. Zaman, J. P. Butler, D. A. Weitz, J. J. Fredberg, and X. Trepat, Nat. Mater. **10**, 469 (2011).
[81] R. E. Peierls, Ann. Inst. Henri Poincaré **5**, 177.
[82] N. D. Mermin, Phys. Rev. **176**, 250 (1968).
[83] A. Nakajima and S. Ishihara, New J. Phys. **13**, 033035 (2011).
[84] H. Kuwayama, S. Ishida, and P. J. M. V. Haastert, J. Cell Biol. **123**, 1453 (1993).
[85] H. Kuwayama, G. T. Viel, S. Ishida, and P. J. M. V. Haastert, Biochim. Biophys. Acta **1268**, 214 (1995).
[86] H. Kuwayama and S. Ishida, Sci. Rep. **3**, 2272 (2013).